

Classification of stable three-dimensional Dirac semimetals with nontrivial topology

Bohm-Jung Yang¹ and Naoto Nagaosa^{1,2}

¹ *RIKEN Center for Emergent Matter Science (CEMS),*

Wako, Saitama 351-0198, Japan and

² *Department of Applied Physics, University of Tokyo, Tokyo 113-8656, Japan*

(Dated: April 4, 2014)

Abstract

A three-dimensional (3D) Dirac semimetal is the 3D analog of graphene whose bulk band shows a linear dispersion relation in the 3D momentum space. Since each Dirac point with four-fold degeneracy carries a zero Chern number, a Dirac semimetal can be stable only in the presence of certain crystalline symmetries. In this work, we propose a general framework to classify stable 3D Dirac semimetals. Based on symmetry analysis, we show that various types of stable 3D Dirac semimetals exist in systems having the time-reversal, inversion, and uniaxial rotational symmetries. There are two distinct classes of stable 3D Dirac semimetals. In the first class, a pair of 3D Dirac points locate on the rotation axis, away from its center. Moreover, the 3D Dirac semimetals in this class have nontrivial topological properties characterized by 2D topological invariants, such as the Z_2 invariant or the mirror Chern number. These 2D topological indices give rise to stable 2D surface Dirac cones, which can be deformed to Fermi arcs when the surface states couple to the bulk states on the Fermi level. On the other hand, the second class of Dirac SM phases possess a 3D Dirac point at a time-reversal invariant momentum (TRIM) on the rotation axis and do not have surface states in general.

A Dirac semimetal (SM) indicates a phase whose low energy excitations can be described by the pseudorelativistic Dirac fermions with the linear energy dispersion. Before the discovery of three dimensional (3D) topological insulators,^{1,2} graphene³ has been considered as the unique system where the intriguing properties of the two dimensional (2D) Dirac fermions can be observed. However, the recent progress in the field of topological insulators has shown that stable 2D Dirac fermions exist ubiquitously on the surface of 3D topological insulators.^{1,2} Moreover, through the careful studies on the topological phase transition between a 3D topological insulator and a normal insulator,⁴⁻⁸ it is demonstrated that even the 3D Dirac fermions with the linear dispersion in all three momentum directions can be observed in the same material if we can reach the quantum critical point. Since the 3D Dirac point with four-fold degeneracy does not carry a topological number, the degeneracy at the gap-closing point can be easily lifted by small external perturbations, hence the 3D Dirac fermions can be observed only at the single quantum critical point. However, the approach to the quantum critical point requires the intricate fine-tuning of the alloy chemical compositions,^{7,8} which limits the accessibility to the fascinating physics of 3D Dirac fermions in experiments.

The breakthrough in the search for stable 3D Dirac semimetals is achieved in the recent series of studies on Na_3Bi ^{9,10} and Cd_3As_2 ¹¹⁻¹³ compounds where a pair of 3D bulk Dirac points stably exist on the k_z axis. The stability of the 3D Dirac points in these materials stems from the fact that the system has additional crystalline symmetries other than the time-reversal symmetry (TRS) and inversion symmetry (IS). For instance, Young et al.^{14,15} have proposed that particular space groups allow 3D Dirac points as symmetry protected degeneracies. Also Wang et al. have shown the symmetry protection of the 3D Dirac points through the detailed symmetry analysis of Na_3Bi ¹⁶ and Cd_3As_2 .¹⁷

In the present paper, we propose a general framework to classify stable 3D Dirac SMs in systems with TRS, IS and uniaxial rotation symmetry, which are the most common symmetries of crystalline solids. Through the careful examination of the condition for the accidental band crossing (ABC), we have accomplished the complete classification of stable 3D Dirac SMs, and uncovered that there is a class of 3D Dirac SMs which have nontrivial topological properties. In particular, we have clarified the fundamental relationship between the crystalline symmetries and the topological property of 3D Dirac SMs, and demonstrated that the 3D *topological* Dirac SM generally mediates the topological quantum phase transition

between a 3D *weak* topological insulator and a normal insulator. In fact, the 3D topological Dirac SM itself is a parent state of 3D topological insulators, which turns into either a 3D strong topological insulator^{16,17} or a 3D topological crystalline insulator when the 3D Dirac point acquires a mass gap due to symmetry breaking.

Results

Basic principles to create 3D Dirac SMs. Our strategy to synthesize a 3D Dirac SM is as follows. Let us consider a system having both the TRS and IS. In general, the TRS requires $E_{n,\uparrow}(\mathbf{k}) = E_{n,\downarrow}(-\mathbf{k})$ where $E_{n,\sigma}(\mathbf{k})$ indicates the energy eigenvalue of the n -th band with the spin $\sigma = \uparrow, \downarrow$ at the momentum \mathbf{k} . On the other hand, the IS requires $E_{n,\sigma}(\mathbf{k}) = E_{n,\sigma}(-\mathbf{k})$. Therefore under the combined operation of TRS and IS, $E_{n,\uparrow}(\mathbf{k}) = E_{n,\downarrow}(\mathbf{k})$, hence the energy band is doubly degenerate locally at each \mathbf{k} . Under this condition, whenever an ABC occurs between the valence and conduction bands, a 3D Dirac point (DP) with four-fold degeneracy can be generated. According to Murakami et al.,⁴⁻⁶ such an ABC can be achieved only under certain limited conditions because of the strong repulsion between degenerate bands. Namely, only when the valence and conduction bands have the opposite parities, an ABC can occur at a time-reversal invariant momentum (TRIM) by tuning an external parameter m . In this case, a 3D DP appears at the quantum critical point ($m = m_c$) between a normal insulator and a Z_2 topological insulator. (See Figure 1a.) Since a band gap opens immediately once $m \neq m_c$, the DP is unstable. However, in many crystals, the rotational symmetry as well as TRS and IS present ubiquitously and constrain the physical properties of materials. Surprisingly, as we will describe in detail below, the additional uniaxial rotational symmetry strongly modifies the condition for ABC, which allows the 3D Dirac SM to emerge as a *stable phase*. This is possible because when the valence and conduction bands have different rotation eigenvalues, the level repulsion between them can be significantly relaxed as pointed out by Wang et al.,^{16,17} which eventually leads to the emergence of a stable 3D Dirac SM phase in the wide range of the parameter space. (See Figure 1b and c.)

To describe an ABC of two bands, each of which is doubly degenerate due to the simultaneous presence of TRS and IS, a 4×4 matrix Hamiltonian can be used as a minimal

Hamiltonian, which in general has the following form,

$$H(\mathbf{k}) = \sum_{i,j=0}^3 a_{ij}(\mathbf{k})\sigma_i\tau_j = \begin{pmatrix} h_{\uparrow\uparrow}(\mathbf{k}) & h_{\uparrow\downarrow}(\mathbf{k}) \\ h_{\downarrow\uparrow}(\mathbf{k}) & h_{\downarrow\downarrow}(\mathbf{k}) \end{pmatrix},$$

where the Pauli matrix $\sigma_{1,2,3}$ ($\tau_{1,2,3}$) indicates the spin (orbital) degrees of freedom and σ_0 and τ_0 are the 2×2 identity matrices. $h_{\sigma\sigma'}$ ($\sigma, \sigma' = \uparrow, \downarrow$) indicates a 2×2 matrix which can be spanned by $\tau_{0,1,2,3}$ and $a_{ij}(\mathbf{k})$ are real functions of \mathbf{k} . The invariance of the system under the C_n rotation gives $C_n H(\mathbf{k}) C_n^{-1} = H(R_n \mathbf{k})$ where R_n is the 3×3 rotation matrix defining the $2\pi/n$ rotation in the 3D space.¹⁸ Without loss of generality, we can choose the k_z axis as the axis of the C_n rotation. Then along the k_z axis on which $R_n \mathbf{k} = \mathbf{k}$ is satisfied, $[C_n, H(\mathbf{k})] = 0$. Therefore we can choose a basis in which both $H(k_z)|_{k_x=k_y=0}$ and C_n are diagonal, hence all bands on the k_z axis can be labeled by the corresponding eigenvalues of C_n . In such a basis, the Hamiltonian can be written as $H(k_z)|_{k_x=k_y=0} = d_0 + d_1\sigma_3 + d_2\tau_3\sigma_3 + d_3\tau_3$ where $d_{0,1,2,3}(k_z, m)$ are real functions. Since the simultaneous presence of TRS and IS requires the double degeneracy of each state, among $d_{1,2,3}$, only one function can be nonzero. Also, since the degenerate bands should have the opposite spin directions, $d_1 = 0$. Hence the Hamiltonian becomes $H(k_z)|_{k_x=k_y=0} = d_0 + d(k_z, m)\Gamma$ where Γ is either $\Gamma = \tau_3$ or $\Gamma = \sigma_3\tau_3$. Then since the energy gap is given by $2|d(k_z, m)|$, an ABC can be achieved if and only if $d(k_z, m) = 0$. Here the number of variables (two) is larger than the number of equations (one) to be satisfied for the band crossing, hence the Dirac SM can always be created via an ABC.

Moreover, due to the TRS and IS, $d(k_z)$ has a definite parity under the sign reversal of k_z as shown in Methods section. In fact, the parity of $d(k_z)$ can be simply determined by the matrix representation P of the IS. Namely, when P has a diagonal form such as $P = \pm\tau_0$ or $\pm\tau_z$, $d(k_z)$ is even while it is odd if P has an off-diagonal form $P = \pm\tau_x$. At first, when $d(k_z)$ is even, $d(k_z) \approx M + \frac{1}{2}t_z k_z^2$ in the leading order with constants M and t_z . In this case, the system is a gapped insulator (a Dirac SM) when $Mt_z > 0$ ($Mt_z < 0$). Namely, by taking M as a tunable parameter and assuming $t_z < 0$, the transition from an insulator ($M < 0$) to a 3D Dirac SM ($M > 0$) can be achieved across the sign reversal of M (or the band inversion). In particular, the 3D Dirac SM phase possesses two DPs which are symmetrically located with respect to the center of the rotation axis at $k_z = \pm\sqrt{2M/|t_z|}$. The Dirac SMs realized in Cd_3As_2 and Na_3Bi belong to this class.^{16,17} On the other hand, when $d(k_z)$ is odd, $d(k_z) \approx vk_z$ in the leading order with a constant v . In this case, there

is a single 3D Dirac point at the center of the k_z axis, i.e., at $k_z = 0$. Then the system is nothing but a stable 3D Dirac SM with a single DP at the center of the rotation axis. Considering the full periodic structure of the Brillouin zone (BZ), both $k_z = 0$ and $k_z = \pi$, i.e., the TRIMs on the rotation axis, are the possible locations of the DP. The candidate Dirac SM systems such as β -cristobalite BiO_2 ¹⁴ and distorted spinels¹⁵ proposed by the recent theoretical studies belong to this class. In fact, there are multiple bulk Dirac points in β -cristobalite BiO_2 due to the crystalline symmetry. However, each Dirac point locates at a TRIM on a rotation axis consistent with our theory. In conclusion, when the material has the TRS, IS, and uniaxial rotation symmetry simultaneously, there are two different ways to obtain a stable Dirac SM phase. One is through the transition from an insulator to a Dirac SM via an ABC, which gives rise to a stable 3D Dirac SM with a pair of 3D bulk DPs on the axis of the rotation. (See Figure 1c.) The other case is when the system naturally supports a 3D DP at a TRIM on the rotation axis due to the symmetry of the system. (See Figure 1b.) The intrinsic properties of the relevant 3D Dirac SM phases are summarized in Table 1 and Table 2, respectively.

Classification table. The classification of the 3D Dirac SM phases can be performed rigorously by imposing the TRS, IS and C_n rotation symmetry to the minimal 4×4 Hamiltonian $H(\mathbf{k})$. In the simultaneous presence of the TRS and IS, the Hamiltonian can always be written as $H(\mathbf{k}) = \sum_{i=1}^5 a_i(\mathbf{k})\Gamma_i$ where Γ_i indicates 4×4 hermitian matrices satisfying $\{\Gamma_i, \Gamma_j\} = 2\delta_{ij}$, which guarantees the double degeneracy of eigenstates at each \mathbf{k} . (See Methods.) The precise functional form of $a_i(\mathbf{k})$ can be fixed by imposing the C_n rotational symmetry using the basis under which both C_n and $H(\mathbf{k})$ are diagonal along the k_z direction.¹⁸ The results of the complete classification are concisely summarized in Table 1 and 2. Because of the TRS, the rotation operator becomes $C_n = \text{diag}[u_{A,\uparrow}, u_{B,\uparrow}, u_{A,\uparrow}^*, u_{B,\uparrow}^*]$ where each component u can be written as $u = \exp[i\frac{2\pi}{n}(p + \frac{1}{2})]$ with $p = 0, 1, \dots, n - 1$ and A, B indicate the orbital degrees of freedom. Hence only two components of C_n are independent.

The properties of the 3D Dirac SM generated via ABCs are shown in Table 1. In general, the ABC requires the valence and conduction bands to have different C_n eigenvalues. Namely, $\{u_{A,\uparrow}, u_{A,\downarrow}\}$ and $\{u_{B,\uparrow}, u_{B,\downarrow}\}$ should not have common elements to avoid the interband hybridization. However, in the case of C_2 invariant systems, $\{u_{A,\uparrow}, u_{A,\downarrow}\} = \{u_{B,\uparrow}, u_{B,\downarrow}\} = \{i, -i\}$, hence the ABC is not allowed for the C_2 invariant systems. On the other hand, the systems with C_3 , C_4 , and C_6 symmetries can support 3D Dirac SM phases.

Although the detailed structure of the Hamiltonian $H(\mathbf{k})$ depends on the specific symmetries of the corresponding system, there are only two different types of low energy effective Hamiltonians near the bulk gap-closing point. In the first case, after some suitable unitary transformations, the effective Hamiltonian near each of the bulk DP can be written as

$$H_{\text{Dirac}}(\mathbf{q}) \sim \begin{pmatrix} q_x\tau_x + q_y\tau_y + q_z\tau_z & 0 \\ 0 & -q_x\tau_x - q_y\tau_y - q_z\tau_z \end{pmatrix},$$

where the momentum \mathbf{q} is measured with respect to the DP. This is the Hamiltonian for the conventional Dirac fermion (the linear Dirac fermion) which is composed of two Weyl fermions having the Chern number $+1$ or -1 , respectively. On the other hand, in the case of the C_6 invariant system with the $\{u_{A,\uparrow}, u_{B,\uparrow}\} = \{e^{i\frac{5\pi}{6}}, e^{i\frac{\pi}{6}}\}$, the effective Dirac Hamiltonian is given by

$$H_{\text{Dirac}}(\mathbf{q}) \sim \begin{pmatrix} (q_x^2 - q_y^2)\tau_x + 2q_xq_y\tau_y + q_z\tau_z & 0 \\ 0 & -(q_x^2 - q_y^2)\tau_x - 2q_xq_y\tau_y - q_z\tau_z \end{pmatrix}.$$

Note that this Dirac point is composed of two double Weyl fermions which have the Chern number $+2$ or -2 , respectively.^{18,19} Hence we call this gapless fermions as the quadratic Dirac fermions. It is worth to stress that one intriguing common property shared by the 3D Dirac SMs created via ABCs is that each Dirac SM possesses a quantized 2D topological invariant, which gives rise to 2D Dirac fermions localized on the surface. The physical origin of such a nontrivial topological property of the 3D Dirac SM phase is described in the following section.

The physical properties of the 3D Dirac SM with a Dirac point at the center of the rotation axis are summarized in Table 2. Since the IS flips the orbitals in this case ($P = \pm\tau_x$), the doubly degenerate states at each momentum on the k_z axis have different orbitals and opposite spin directions. Therefore the band crossing between degenerate bands requires $\{u_{A,\uparrow}, u_{B,\downarrow}\} \cap \{u_{B,\uparrow}, u_{A,\downarrow}\} = \emptyset$ contrary to the previous case. Moreover, due to the additional constraint of $u_{A,\uparrow} = -u_{B,\uparrow}$, the Dirac SM phase with a single DP cannot exist in the system with C_3 invariance while the systems with C_2 , C_4 , C_6 symmetries support it. (See Methods.) Since the DP locates in the $k_z = 0$ plane, the quantized 2D topological invariant cannot be defined in the same plane, hence we do not expect any surface state in this class of the 3D Dirac SMs in general. One interesting prediction of Table 2 is that when the system has C_6

symmetry with $u_{A,\uparrow} = \pm e^{i\frac{3\pi}{6}}$, the low energy Hamiltonian near the DP can be written as

$$H_{\text{Dirac}}(\mathbf{q}) \sim \begin{pmatrix} (q_+^3 + q_-^3)\tau_x + i(q_+^3 - q_-^3)\tau_y + q_z\tau_z & 0 \\ 0 & -(q_+^3 + q_-^3)\tau_x - i(q_+^3 - q_-^3)\tau_y - q_z\tau_z \end{pmatrix}.$$

Note that this Dirac point is composed of two triple Weyl fermions which have the Chern number $+3$ or -3 , respectively.¹⁸ Hence we can call this gapless fermion as the cubic Dirac fermion. For the other cases in Table 2, the effective Hamiltonian near the DP is simply described by the ordinary linear Dirac fermions.

Topological properties of the 3D Dirac SM. One important characteristic of the 3D Dirac SM generated by an ABC is that it carries a quantized topological invariant although it is a gapless SM. In fact, the band inversion associated with the ABC is the common origin of the presence of the 2D topological invariant and the emergence of bulk DPs. As shown in Table 1, in each case, a quantized 2D topological invariant can be defined on the $k_z = 0$ plane where the ABC occurs. First of all, since the $k_z = 0$ plane can be considered as a 2D system with TRS, a 2D Z_2 invariant ν_{2D} is well-defined on it.^{20,21} Moreover, because of the simultaneous presence of the TRS and IS, ν_{2D} can be determined by the parities of the occupied bands at the time reversal invariant momenta.²² Therefore when the valence and conduction bands have the opposite parities ($P = \pm\tau_z$), the band inversion on the $k_z = 0$ plane, which generates a pair of bulk DPs, changes ν_{2D} by 1, i.e., $\Delta\nu_{2D} = 1$. This can be contrasted to the case when two bands have the same parity ($P = \pm\tau_0$), in which $\Delta\nu_{2D} = 0$ in spite of the occurrence of the band inversion.

On the other hand, when the system has either C_4 or C_6 symmetry, the $k_z = 0$ plane carries an integer topological invariant (the mirror Chern number) due to the mirror symmetry of the system.^{23,24} Here the mirror symmetry appears due to the simultaneous presence of the π rotation (R_π) with respect to the k_z axis and the IS. Then the combined operation of the IS and π rotation defines the mirror symmetry $M = PR_\pi$, which connects the Hamiltonian $H(k_x, k_y, k_z)$ and $H(k_x, k_y, -k_z)$, hence the system is invariant under the mirror symmetry (M) in the $k_z = 0$ plane. Since $M^2 = -1$, the Hamiltonian can be block-diagonalized with each block characterized by the mirror eigenvalue $\pm i$, respectively. Then the Chern number can be defined in each block ($C_{\pm i}$), separately. Although the total Chern number $C_{+i} + C_{-i} = 0$ due to the TRS, the difference $n_M \equiv \frac{1}{2}(C_i - C_{-i})$ (the mirror Chern number) can be nonzero. Note that R_π exists only in systems with the C_4 or C_6 symmetry with

the corresponding $R_\pi = C_4^2$ or $R_\pi = C_6^3$, respectively. Therefore the C_3 invariant system is characterized only by the 2D Z_2 invariant ν_{2D} while the system with the C_4 or C_6 symmetry has both the Z_2 invariant ν_{2D} and the mirror Chern number n_M where n_M and ν_{2D} are equivalent up to the modulo 2. In Methods section, we have described how the mirror symmetry manifests in the system in terms of the effective Hamiltonian $H(\mathbf{k})$.

When either ν_{2D} or n_M is nonzero, the 3D Dirac SM supports 2D surface Dirac cones when a surface parallel to the k_z axis is introduced. The number of 2D Dirac cones on one surface is given by $|n_M|$ ($|\nu_{2D}|$) when the system has the C_4 or C_6 (C_3) symmetry. The typical surface spectrum is composed of two parts. One is from the 3D bulk Dirac states projected to the surface BZ and the other is from the 2D surface Dirac cones resulting from the 2D topological index. When these two contributions are decoupled on the Fermi level, the 2D Dirac cone forms an isolated closed loop. On the other hand, when the bulk and surface states are coupled on the Fermi level, the 2D surface states form Fermi arcs connecting the bulk states. The precise shape of the Fermi surface in the surface BZ depends on the symmetry of the system and detailed material parameters.

It is worth to stress that the physical origin of the surface Fermi arcs in the 3D Dirac SM is clearly distinct from that of the Weyl SM which has two-fold degeneracy at the gap-closing point. In the Weyl SM, the Chern number carried by the bulk gapless point (Weyl point) guarantees the emergence and stability of the Fermi arc states.²⁵⁻²⁷ Since the Chern number of the Weyl point is purely determined by the energy dispersion around the Weyl point, the number of Fermi arcs in the system with a fixed number of Weyl points strongly depends on the energy dispersion near the Weyl point. In conventional Weyl SMs with the linear dispersion around the Weyl point, the number of Fermi arcs on one surface of the sample is equal to the number of Weyl point pairs in the first BZ. On the other hand, in the case of Weyl SMs with double (triple) Weyl fermions whose dispersion is quadratic (cubic) along the two momentum directions but linear in the third direction, the number of Fermi arcs is double (triple) of the number of the Weyl point pairs.^{18,19} However, in contrast to the case of the Weyl SM, the physical origin of the surface states of the 3D Dirac SM is independent of the energy dispersion of the 3D bulk Dirac fermions. Because of the simultaneous presence of the TRS and IS, the Chern number of each 3D Dirac point is zero, hence the 3D Dirac point is topologically trivial. Here the number of the Fermi arcs on the surface of the sample is solely determined by the 2D topological invariant on the $k_z = 0$ (or $k_z = \pi$) plane

irrespective of the energy dispersion around the 3D bulk Dirac points. Therefore although the low energy Hamiltonian near the 3D bulk Dirac point is the same, the number of Fermi arcs can be different depending on the 2D topological invariant of the system. An example is shown in Figure 3.

Lattice model and generic phase diagram. Let us illustrate the intriguing properties of the 3D topological Dirac SM phases in Table 1 by studying lattice Hamiltonians numerically. For convenience, we choose the C_4 invariant systems with $P = \tau_0$ (Equation (17) in Methods.) or $P = \tau_z$ (Equation (14) in Methods.) corresponding to the 6th or 7th row of Table 1, respectively. However, the main features of the phase diagram can be applied to all cases in Table 1 because the overall structure of the phase diagram is solely determined by the single function $a_5(\mathbf{k})$ whose leading order functional form is the same in all cases. The detailed information about the lattice Hamiltonian is presented in the Methods section. Figure 2 summarizes the main properties of the lattice Hamiltonian. In general, the system supports four different phases as shown in the phase diagram. The phase transition is always accompanied by an ABC on the $k_z = 0$ or $k_z = \pi$ plane in which a pair of 3D bulk DPs are either created or annihilated. Whenever an ABC happens, it changes the 2D topological invariant of the corresponding 2D planes. When any of these 2D planes has a nonzero topological invariant, the system supports 2D Dirac fermions on the surface which is parallel to the rotation axis.

There are two different types of insulators in the phase diagram. One is a normal insulator which does not carry a topological number, and the other is a weak topological insulator in which both the $k_z = 0$ and $k_z = \pi$ planes have nontrivial 2D topological invariants. In systems with $P = \pm\tau_z$, the weak topological insulator is equivalent to the conventional weak topological insulator with the Z_2 topological index $(\nu_0; \nu_1\nu_2\nu_3) = (0; 001)$ because $\nu_{2D} = 1$ in both the $k_z = 0$ and $k_z = \pi$ planes. On the other hand, when $P = \pm\tau_0$, the nature of the weak topological insulator in the phase diagram is unconventional in the sense that the topological property of the insulator is determined by the nonzero mirror Chern number $n_M = 2$ on both the $k_z = 0$ and $k_z = \pi$ planes.

The 3D Dirac SM phases can also be distinguished in two different ways. At first, when the Dirac SM phase has a nonzero topological invariant in either the $k_z = 0$ plane or the $k_z = \pi$ plane, we can call it a *topological Dirac SM* since the Dirac SM carries stable 2D Dirac cones on the surface. Similarly, a topologically trivial Dirac SM can be defined when

the system does not have any topological invariant in both planes. However, in both cases, independent of the presence of the 2D topological invariants, the 3D Dirac SM phase is stable due to the symmetry of the system and occupies a finite region in the phase diagram.

Figure 3 shows the evolution of the Fermi surface of the topological Dirac SM system with a slab geometry whose surface normal is parallel to the $[100]$ direction. The translational symmetry of the system in the yz plane is maintained. Here we first pick the states touching the Fermi level (E_F) and then plot the wave function amplitudes of the corresponding state localized on the first five layers from the top surface. The red color indicates the states localized on the $[100]$ surface while the bright blue color corresponds to the 3D bulk Dirac states. In the case of the topological Dirac SM with $\nu_{2D} = 1$ in the $k_z = 0$ plane, a 2D surface Dirac cone appears on the k_y axis centered at the Γ point as shown in Figure 3a. Here the two bulk Dirac points give rise to the finite intensity on the k_z axis located symmetrically with respect to the Γ point. When the Fermi energy (E_F) is near the bulk Dirac point ($E_F = 0$ at the bulk Dirac point), the bulk and surface states are decoupled, and the surface states form an isolated closed loop. As E_F increases, the Fermi surface topology evolves continuously, and when the bulk and surface states start to overlap, the 2D surface state is deformed to the Fermi arc structure. Namely, the Fermi arcs of 3D Dirac SM emerge simply because of the deformation of the 2D Dirac cone which exists due to the fact that $\nu_{2D} = 1$ on the $k_z = 0$ plane. Since such an evolution of the surface spectrum occurs continuously, the Fermi arc states can appear even when $E_F = 0$ if the parameters of the model Hamiltonian are tuned properly.

The energy spectrum of the topological Dirac SM with $n_M = 2$ on the $k_z = 0$ plane also shows a similar variation as described in Figure 3b. Since $n_M = 2$, there are two 2D surface Dirac cones on the k_y axis. As E_F increases, the surface Dirac cones evolve to Fermi arcs when the surface and bulk states overlap. Since the number of surface Dirac cones is two, the number of surface Fermi arc is also doubled as compared to the case shown in Figure 3a. It is worth to note that in both cases shown in Figure 3a and 3b, the energy dispersion near the bulk 3D Dirac point is basically the same, i.e., the bulk state shows the linear dispersion relation in all three momentum directions. This clearly shows that the number of Fermi arcs of the topological Dirac SM is irrespective of the dispersion of the bulk states.

Discussion

Let us illustrate the role of the rotational symmetry by comparing the Figure 1a-c. When the system has the TRS and IS without the rotational symmetry, corresponding to Figure 1a, the 3D DP appears at the quantum critical point between the normal insulator and the strong topological insulator. Since the 3D DP can be observed only at the single point of the phase diagram, the Dirac SM is not a stable phase in this case. On the other hand, in the presence of the additional uniaxial rotational symmetry, two different types of phase diagrams emerge as shown in Figure 1b and 1c. In both cases, the Dirac SM is a stable phase occupying a finite region of the phase diagram. At first, due to the rotation symmetry, the Dirac point can persist at a TRIM on the rotation axis independent of the external control parameter m , hence there is only a single phase in the phase diagram as shown in Figure 1b. The Dirac SMs in Table 2 correspond to this case. Whereas, when the Dirac SM is generated via an ABC, the phase diagram is depicted in Figure 1c and the properties of the corresponding Dirac SM are summarized in Table 1. In fact, the 3D topological Dirac SM phase emerging here can also be understood as a state intermediating a topological phase transition between two insulators. Namely, the 3D topological Dirac SM mediates the transition between a normal insulator and a weak topological insulator. At the critical points, a pair of 3D DPs are either created ($m = m_{c1}$) or annihilated ($m = m_{c2}$) at the center or the boundary of the rotation axis, respectively. Between the two critical points, as m increases, the pair of 3D DPs move along the rotation axis in the opposite directions, and finally recombine when they hit the BZ boundary. Since each DP is stable due to the symmetry of the system, the pair creation or the pair annihilation is the only way to change the number of the DPs as long as the TRS, IS, and rotation symmetry are present at the same time.

Since the four-fold degeneracy at the DP is protected by symmetries, it is important to understand the fate of the 3D Dirac SM under symmetry breaking perturbations. In particular, it is worth to note that the 3D topological Dirac SM itself can be considered as a parent state of various topological insulators that can be obtained when the DP acquires a mass gap by breaking the rotation symmetry. When the topological Dirac SM carries a nontrivial 2D Z_2 invariant on either the $k_z = 0$ or the $k_z = \pi$ plane, the Dirac SM turns into a Z_2 strong topological insulator as long as the perturbation does not break the time

reversal symmetry. Also in the case of the topological Dirac SM with a nonzero mirror Chern number, it becomes a topological crystalline insulator after the gap opening, as long as the mirror symmetry of the system is not broken in the presence of the perturbations.

We conclude with a discussion about the stability of the 3D Dirac SM under the influence of the Coulomb interaction and disorder. Simple power counting shows that the long range Coulomb interaction is a marginally irrelevant perturbation to the 3D Dirac fermions with the linear dispersion.²⁸⁻³⁰ Hence various physical properties of the 3D Dirac SM can receive logarithmic corrections due to the long range Coulomb interaction similar to the cases of 3D Weyl SM²⁹⁻³¹ and graphene.³²⁻³⁴ On the other hand, since the disorder is irrelevant according to the power counting, we expect the Dirac SM state can be stable at least against weak disorder effect. However, since the crystalline symmetry is important for the protection of the DP, strong disorder can induce nontrivial physical consequences to 3D Dirac SM phase, especially when the interaction and disorder effect are considered simultaneously.²⁸ Moreover, in the case of the quadratic Dirac SM and the cubic Dirac SM, the effect of the interaction and disorder can be more significant. Since the in-plane dispersion becomes either quadratic or cubic in the momentum space, which strongly enhances the low energy density of states, it is expected that the interaction and disorder can even bring about new exotic quantum phases. For instance, according to a recent theoretical study, an exotic non-Fermi liquid state can appear in a 3D semimetal having quadratic energy dispersion in the momentum space.³⁵ Since the interplay between the long-range Coulomb interaction and nontrivial screening due to the enhanced low energy density of states is the fundamental origin leading to the non-Fermi liquid phase, the quadratic Dirac SM and the cubic Dirac SM are also promising systems to observe novel quantum critical states.

Finally, let us note that the quantum critical point in Figure 1c where the pair creation or pair annihilation of bulk DPs happens is another interesting venue to observe a new types of quantum critical phenomena. At the quantum critical point, since the energy dispersion along the rotation axis is always quadratic, the low energy excitation can show highly anisotropic dispersion relations in the linear Dirac SM and cubic Dirac SM. According to the recent theoretical study,^{36,37} it is shown that such an anisotropic dispersion can induce a novel screening phenomenon which can induce anomalous distribution of the screening charge around a charged impurity. To reveal the fascinating physical properties of the linear Dirac SM and the triple Dirac SM at the critical point would be another interesting topic

for future studies.

Methods

The classification procedure. The classification of the minimal 4×4 matrix Hamiltonian $H(\mathbf{k})$ can be performed as follows. At first, let us impose the TRS on $H(\mathbf{k})$. The TRS can be represented by the operator $\Theta = i\sigma_y K$ where $\sigma_{x,y,z}$ are Pauli matrices for spin degrees of freedom and K stands for complex conjugation. The invariance of the Hamiltonian under TRS, i.e., $H(-\mathbf{k}) = \Theta H(\mathbf{k}) \Theta^{-1}$ gives rise to the relations $h_{\uparrow\uparrow}(\mathbf{k}) = h_{\downarrow\downarrow}^T(-\mathbf{k})$ and $h_{\uparrow\downarrow}(\mathbf{k}) = -h_{\uparrow\downarrow}^T(-\mathbf{k})$ where the superscript T indicates the transposition. Then the resulting Hamiltonian with the TRS can be written in the following way.

$$H(\mathbf{k}) = \begin{pmatrix} h_{\uparrow\uparrow}(\mathbf{k}) & h_{\uparrow\downarrow}(\mathbf{k}) \\ -h_{\uparrow\downarrow}^*(-\mathbf{k}) & h_{\uparrow\uparrow}^*(-\mathbf{k}) \end{pmatrix},$$

where the superscript $*$ indicates the complex conjugation. Secondly, to impose the IS on the Hamiltonian $H(\mathbf{k})$, we have to determine the matrix representation P of the IS. Since the IS is independent of the spin-rotation, in general $P = p_0\tau_0 + \vec{p} \cdot \vec{\tau}$ where $\vec{\tau} = (\tau_x, \tau_y, \tau_z)$ indicate the Pauli matrices for orbital degrees of freedom and $p_{0,x,y,z}$ are complex numbers. Since the operation of P^2 relates the same electronic states, it should be equivalent to the identity operator up to a global U(1) phase factor, i.e., $P^2 = p_0^2 + \vec{p} \cdot \vec{p} + 2p_0\vec{p} \cdot \vec{\tau} = e^{i2\phi}$. Therefore P should be either $P = \pm e^{i\phi}$ or $P = e^{i\phi} \vec{p}' \cdot \vec{\tau}$ where $\vec{p}' \cdot \vec{p}' = 1$. To determine ϕ and \vec{p}' , the following three relations can be used. (i) $[T, P] = 0$, (ii) $P^\dagger P = 1$, and (iii) $(TP)^2 = -1$. Then the general solution for P is given by $P = \pm\tau_0$ or $P = \cos\theta\tau_z - \sin\theta\tau_x$ with $\theta \in [0, 2\pi]$.

The invariance of the Hamiltonian under P , i.e., $H(-\mathbf{k}) = PH(\mathbf{k})P^{-1}$ combined with the TRS constrains the possible form of the Hamiltonian, which can be summarized in the following way.

(a) When $P = \pm\tau_0$. $H(\mathbf{k}) = a_0(\mathbf{k}) + \sum_{i=1}^5 a_i(\mathbf{k})\Gamma_i$ where $\Gamma_1 = \tau_x$, $\Gamma_2 = \tau_y\sigma_z$, $\Gamma_3 = \tau_y\sigma_x$, $\Gamma_4 = \tau_y\sigma_y$, $\Gamma_5 = \tau_z$. Hence $h_{\uparrow\uparrow} = a_0 + a_1\tau_x + a_2\tau_y + a_5\tau_z$ and $h_{\uparrow\downarrow} = (a_3 - ia_4)\tau_y$. Here $a_{0,1,2,3,4,5}(\mathbf{k})$ are all real and even under the sign change of \mathbf{k} .

(b) When $P = \cos\theta\tau_z - \sin\theta\tau_x$. $H(\mathbf{k}) = a_0(\mathbf{k}) + \sum_{i=1}^5 a_i(\mathbf{k})\Gamma_i$ where $\Gamma_1 = \mu_x\sigma_z$, $\Gamma_2 = \mu_y$, $\Gamma_3 = \mu_x\sigma_x$, $\Gamma_4 = \mu_x\sigma_y$, $\Gamma_5 = \mu_z$, and all $a_{0,1,2,3,4,5}$ are real functions. Hence $h_{\uparrow\uparrow} = a_0 + a_1\mu_x +$

$a_2\mu_y + a_5\mu_z$ and $h_{\uparrow\downarrow} = (a_3 - ia_4)\mu_x$. Here $a_{0,5}(-\mathbf{k}) = a_{0,5}(\mathbf{k})$, $a_{1,2,3,4}(-\mathbf{k}) = -a_{1,2,3,4}(\mathbf{k})$, and $\mu_x = \cos\theta\tau_x + \sin\theta\tau_z$, $\mu_y = \tau_y$, $\mu_z = -\sin\theta\tau_x + \cos\theta\tau_z$.

In both cases, an ABC is possible only if the five equations $a_{1,2,3,4,5} = 0$ are satisfied simultaneously. Here each function a_i has four variables including the three momentum components $k_{x,y,z}$ and one external control parameter m , i.e., $a_i = a_i(k_x, k_y, k_z, m)$. Since the number of equations to be satisfied is five while the number of variables is four, the condition for the ABC cannot be satisfied in general at a generic momentum \mathbf{k} . However, it is worth to note that the above consideration does not rule out the ABC at non-generic points in the momentum space with high symmetry. For instance, as pointed out by Murakami,⁴ at the time reversal invariant momentum $\mathbf{k} = \mathbf{k}_{\text{TRIM}}$ where \mathbf{k} and $-\mathbf{k}$ are equivalent, all odd functions in $H(\mathbf{k})$ vanish. In the case of (b) with $P = \cos\theta\tau_z - \sin\theta\tau_x$, $a_{1,2,3,4}(\mathbf{k}_{\text{TRIM}}) = 0$. Therefore an ABC is possible if and only if one condition $a_5(\mathbf{k}_{\text{TRIM}}, m) = 0$ is satisfied, which can be achieved by tuning one external control parameter m . This is the reason why the topological phase transition between two insulators can occur through an ABC at a time reversal invariant momentum.

Now let us show how the condition for ABC is modified by the presence of the additional rotation symmetry C_n with respect to the z axis. Here n is restricted to be $n = 2, 3, 4, 6$ in periodic lattice systems. Using a basis in which both $H(k_z)|_{k_x=k_y=0}$ and C_n are diagonal, C_n can be represented by a diagonal matrix $C_n = \text{diag}[u_{A,\uparrow}, u_{B,\uparrow}, u_{A,\downarrow}, u_{B,\downarrow}] = \text{diag}[\alpha_p, \alpha_q, \alpha_r, \alpha_s]$ where $\alpha_p = \exp[i\frac{2\pi}{n}(p + \frac{1}{2})]$ with $p = 0, 1, \dots, n-1$.¹⁸ For convenience, we express C_n in the following way,

$$C_n = \begin{pmatrix} e^{i\pi(\frac{1+p+q}{n} + \frac{p-q}{n}\tau_z)} & 0 \\ 0 & e^{i\pi(\frac{1+r+s}{n} + \frac{r-s}{n}\tau_z)} \end{pmatrix}.$$

The invariance of the Hamiltonian under C_n leads to

$$C_n H(k_+, k_-, k_z) C_n^{-1} = H(k_+ e^{i\frac{2\pi}{n}}, k_- e^{-i\frac{2\pi}{n}}, k_z) \quad (1)$$

where $k_{\pm} = k_x \pm ik_y$. From Equation (1), we can obtain that

$$\begin{aligned} e^{i\frac{\pi}{n}(p-q)\tau_z} h_{\uparrow\uparrow}(k_{\pm}) e^{-i\frac{\pi}{n}(p-q)\tau_z} &= h_{\uparrow\uparrow}(k_{\pm} e^{\pm i\frac{2\pi}{n}}), \\ e^{i\frac{\pi}{n}(p+q-r-s)} e^{i\frac{\pi}{n}(p-q)\tau_z} h_{\uparrow\downarrow}(k_{\pm}) e^{i\frac{\pi}{n}(s-r)\tau_z} &= h_{\uparrow\downarrow}(k_{\pm} e^{\pm i\frac{2\pi}{n}}). \end{aligned} \quad (2)$$

The equations above can be further simplified by considering the constraint on C_n due to TRS. Namely, since $[T, C_n] = 0$, we can show that $\exp[i\frac{2\pi}{n}(p+r+1)] = 1$, $\exp[i\frac{2\pi}{n}(q+s+1)] =$

1, and $C_n = \text{diag}[\alpha_p, \alpha_q, \alpha_p^*, \alpha_q^*]$. Namely, $C_n = \text{diag}[u_{A,\uparrow}, u_{B,\uparrow}, u_{A,\downarrow} = u_{A,\uparrow}^*, u_{B,\downarrow} = u_{B,\uparrow}^*]$. Then Equation (2) becomes

$$\begin{aligned} e^{i\frac{\pi}{n}(p-q)\tau_z} h_{\uparrow\uparrow}(k_{\pm}) e^{-i\frac{\pi}{n}(p-q)\tau_z} &= h_{\uparrow\uparrow}(k_{\pm} e^{\pm i\frac{2\pi}{n}}), \\ e^{i\frac{2\pi}{m}(q-r)} e^{i\frac{\pi}{n}(p-q)\tau_z} h_{\uparrow\downarrow}(k_{\pm}) e^{i\frac{\pi}{n}(p-q)\tau_z} &= h_{\uparrow\downarrow}(k_{\pm} e^{\pm i\frac{2\pi}{n}}). \end{aligned} \quad (3)$$

In general, $h_{\uparrow\uparrow}(\mathbf{k})$ and $h_{\uparrow\downarrow}(\mathbf{k})$ can be represented by

$$\begin{aligned} h_{\uparrow\uparrow}(\mathbf{k}) &= f_0(\mathbf{k}) + f_+(\mathbf{k})\tau_+ + f_+^*(\mathbf{k})\tau_- + f_z(\mathbf{k})\tau_z, \\ h_{\uparrow\downarrow}(\mathbf{k}) &= g_0(\mathbf{k}) + g_+(\mathbf{k})\tau_+ + g_-(\mathbf{k})\tau_- + g_z(\mathbf{k})\tau_z, \end{aligned} \quad (4)$$

where $f_{0,z}$ are real functions while $f_+, g_{0,\pm,z}$ are complex functions. Also $\tau_{\pm} = \tau_x \pm i\tau_y$. Since f_0 does not affect the gap-closing, we can neglect it in the forthcoming discussion. Equation (3) gives the following relations,

$$\begin{aligned} e^{i\frac{2\pi}{n}(p-q)} f_+(k_{\pm}, k_z) &= f_+(k_{\pm} e^{\pm i\frac{2\pi}{n}}, k_z), \\ f_z(k_{\pm}, k_z) &= f_z(k_{\pm} e^{\pm i\frac{2\pi}{n}}, k_z), \end{aligned} \quad (5)$$

and

$$\begin{aligned} e^{i\frac{2\pi}{n}(p-r)} g_{0+z}(k_{\pm}, k_z) &= g_{0+z}(k_{\pm} e^{\pm i\frac{2\pi}{n}}, k_z), \\ e^{i\frac{2\pi}{n}(q-s)} g_{0-z}(k_{\pm}, k_z) &= g_{0-z}(k_{\pm} e^{\pm i\frac{2\pi}{n}}, k_z), \\ e^{i\frac{2\pi}{n}(q-r)} g_{\pm}(k_{\pm}, k_z) &= g_{\pm}(k_{\pm} e^{\pm i\frac{2\pi}{n}}, k_z), \end{aligned} \quad (6)$$

where $g_{0\pm z} = g_0 \pm g_z$. The Equations (5) and (6) are the key results which lead to the full classification of the 3D Dirac SM.

For the classification, we first consider the TRS and IS, which restricts the possible structure of the Hamiltonian summarized in (a) and (b). After that the rotational symmetry is imposed to the Hamiltonian by using the Equations (5) and (6). As shown previously, the most general form of P is given by $P = \pm\tau_0$ or $P = \cos\theta\tau_z - \sin\theta\tau_x$ with $\theta \in [0, 2\pi]$. To determine the matrix representation of P and C_n , we use the basis in which both the $H(k_z)|_{k_x=k_y=0}$ and C_n are diagonal. As noted before, in such a basis, the Hamiltonian should have a diagonal form given by $H(k_z)|_{k_x=k_y=0} = d(k_z)\Gamma$ with $\Gamma \in \{\tau_z, \tau_z\sigma_z\}$. Since $d(k_z)$ should have a definite parity under IS as shown in (a) and (b), the possible form of P is restricted to be $P = \pm\tau_0, \pm\tau_x, \pm\tau_z$. In particular, when $P = \pm\tau_0$ or $\pm\tau_z$, $d(\mathbf{k})$ is even

under the sign change of the momentum \mathbf{k} , which leads to the 3D topological Dirac SM via an ABC. (Table 1) On the other hand, when $P = \pm\tau_x$, $d(\mathbf{k})$ is odd under the sign change of \mathbf{k} , which gives rise to a 3D Dirac SM with a single bulk Dirac point. (Table 2)

Let us describe the constraints from the rotation symmetry in detail. When $P = \pm\tau_0$, the Hamiltonian $h_{\uparrow\uparrow}(\mathbf{k})$ and $h_{\uparrow\downarrow}(\mathbf{k})$ are given by

$$\begin{aligned} h_{\uparrow\uparrow}(\mathbf{k}) &= a_1(\mathbf{k})\tau_x + a_2(\mathbf{k})\tau_y + a_5(\mathbf{k})\tau_z, \\ h_{\uparrow\downarrow}(\mathbf{k}) &= (a_3(\mathbf{k}) - ia_4(\mathbf{k}))\tau_y. \end{aligned} \quad (7)$$

On the other hand, when $P = \pm\tau_z$,

$$\begin{aligned} h_{\uparrow\uparrow}(\mathbf{k}) &= a_1(\mathbf{k})\tau_x + a_2(\mathbf{k})\tau_y + a_5(\mathbf{k})\tau_z, \\ h_{\uparrow\downarrow}(\mathbf{k}) &= (a_3(\mathbf{k}) - ia_4(\mathbf{k}))\tau_x. \end{aligned} \quad (8)$$

In both cases, from Equations (5) and (6), we can obtain

$$\begin{aligned} e^{i\frac{2\pi}{n}(p-q)} f_+(k_{\pm}, k_z) &= f_+(k_{\pm}e^{\pm i\frac{2\pi}{n}}, k_z), \\ a_5(k_{\pm}, k_z) &= a_5(k_{\pm}e^{\pm i\frac{2\pi}{n}}, k_z), \\ e^{i\frac{2\pi}{n}(q-r)} g(k_{\pm}, k_z) &= g(k_{\pm}e^{\pm i\frac{2\pi}{n}}, k_z), \end{aligned} \quad (9)$$

where $f_+(\mathbf{k}) = (a_1(\mathbf{k}) - ia_2(\mathbf{k}))/2$ and $g(\mathbf{k}) = (a_3(\mathbf{k}) - ia_4(\mathbf{k}))/2$. Since f_+ and g should be zero on the k_z axis, we obtain $e^{i\frac{2\pi}{n}(p-q)} = u_{A,\uparrow}u_{B,\uparrow}^* \neq 1$ and $e^{i\frac{2\pi}{n}(q-r)} = u_{B,\uparrow}u_{A,\downarrow}^* \neq 1$. Hence the ABC is possible when $\{u_{A,\uparrow}, u_{A,\downarrow}\} \cap \{u_{B,\uparrow}, u_{B,\downarrow}\} = \emptyset$, i.e., when the valence and conduction bands have no rotation eigenvalue in common.

Finally, when $P = \pm\tau_x$, the Hamiltonian $h_{\uparrow\uparrow}(\mathbf{k})$ and $h_{\uparrow\downarrow}(\mathbf{k})$ are given by

$$\begin{aligned} h_{\uparrow\uparrow}(\mathbf{k}) &= a_5(\mathbf{k})\tau_x + a_2(\mathbf{k})\tau_y + a_1(\mathbf{k})\tau_z, \\ h_{\uparrow\downarrow}(\mathbf{k}) &= (a_3(\mathbf{k}) - ia_4(\mathbf{k}))\tau_z. \end{aligned} \quad (10)$$

From the Equations (5) and (6), we can obtain

$$\begin{aligned} e^{i\frac{2\pi}{n}(p-q)} f_+(q_{\pm}, k_z) &= f_+(q_{\pm}e^{\pm i\frac{2\pi}{n}}, k_z), \\ a_1(q_{\pm}, k_z) &= a_1(q_{\pm}e^{\pm i\frac{2\pi}{n}}, k_z), \\ e^{i\frac{2\pi}{n}(p-r)} g_z(q_{\pm}, k_z) &= e^{i\frac{2\pi}{n}(q-s)} g_z(q_{\pm}, k_z) = g_z(q_{\pm}e^{\pm i\frac{2\pi}{n}}, k_z), \end{aligned} \quad (11)$$

where $f_+(\mathbf{k}) = (a_5(\mathbf{k}) - ia_2(\mathbf{k}))/2$ and $g_z(\mathbf{k}) = (a_3(\mathbf{k}) - ia_4(\mathbf{k}))$. From the condition that $f_+ = g_z = 0$ on the k_z axis, we obtain $e^{i\frac{2\pi}{n}(p-q)} = u_{A,\uparrow}u_{B,\uparrow}^* \neq 1$, $e^{i\frac{2\pi}{n}(p-r)} = u_{A,\uparrow}u_{A,\downarrow}^* \neq 1$,

$e^{i\frac{2\pi}{n}(q-s)} = u_{B,\uparrow}u_{B,\downarrow}^* \neq 1$, and $u_{A,\uparrow}^2 = u_{B,\uparrow}^2$. Namely, (i) $\{u_{A,\uparrow}, u_{B,\downarrow}\} \cap \{u_{B,\uparrow}, u_{A,\downarrow}\} = \emptyset$ and (ii) $u_{A,\uparrow} = -u_{B,\uparrow}$ are the two conditions to be satisfied. The physical meaning of these two conditions is as follows. First of all, since the IS flips the orbitals in this case ($P = \pm\tau_x$), $E_{A,\sigma}(k_z) = E_{B,\sigma}(-k_z)$. Then the combined operation of the TRS and IS ensures $E_{A,\uparrow}(k_z) = E_{B,\downarrow}(k_z)$ and $E_{A,\downarrow}(k_z) = E_{B,\uparrow}(k_z)$ on the k_z axis. Note that the orbital index is physically meaningful in this case, because the angular momentum is a good quantum number on the k_z axis. Then the crossing between two degenerate bands requires $\{u_{A,\uparrow}, u_{B,\downarrow}\} \cap \{u_{B,\uparrow}, u_{A,\downarrow}\} = \emptyset$. Moreover, since $(C_n P)^2 = (P C_n)^2$ on the k_z axis, $C_n P = \pm P C_n$. However, since the condition (i) is violated if $[C_n, P] = 0$ is fulfilled, we obtain $\{C_n, P\} = 0$, which immediately leads to the condition (ii). In fact, the condition (ii) $u_{A,\uparrow} = -u_{B,\uparrow}$ means $\exp[i\frac{2\pi}{n}(p + \frac{1}{2})] = -\exp[i\frac{2\pi}{n}(q + \frac{1}{2})]$ with integers p and q . But this relation cannot be satisfied if $n = 3$. Therefore the 3D Dirac SM with a single DP cannot exist in systems with C_3 invariance.

The emergence of the mirror symmetry in the Hamiltonian. Let us briefly describe how the mirror symmetry manifests in the effective Hamiltonian $H(\mathbf{k}) = \sum_{i=1}^5 a_i(\mathbf{k})\Gamma_i$. As shown in Table 1, in systems with the C_4 or C_6 symmetry, either $f(\mathbf{k})$ or $g(\mathbf{k})$ becomes zero in the $k_z = 0$ plane. Although only the lowest order terms are shown in Table 1, we can show that the same result holds in all orders. This means that the effective Hamiltonian can be written as $H(\mathbf{k}) = \sum_{i=1,2,3} a'_i(\mathbf{k})\Gamma'_i$ in the $k_z = 0$ plane. Here $\Gamma'_{1,2,3}$ are three mutually anti-commuting Gamma matrices. Since only three Gamma matrices appear in the Hamiltonian, we can define a conserved quantity $\Gamma'_4\Gamma'_5$ satisfying $[H(\mathbf{k}), \Gamma'_4\Gamma'_5] = 0$. It is straightforward to show that $\Gamma'_4\Gamma'_5$ is equivalent to the mirror operator M in all cases, hence the system has the mirror symmetry in the $k_z = 0$ plane.

The lattice Hamiltonians. We can construct the lattice Hamiltonians straightforwardly by using the information in Table 1 and 2. For instance, for the C_4 invariant system with $P = \pm\tau_z$, i.e., 6-th row of Table 1, we can use

$$\begin{aligned}
f &= \eta(\sin k_x + i \sin k_y), \\
g &= \sin k_z[(\beta + \gamma)(\cos k_y - \cos k_x) + i(\beta - \gamma) \sin k_x \sin k_y], \\
a_5 &= M - t_{xy}(\cos k_x + \cos k_y) - t_z \cos k_z,
\end{aligned} \tag{12}$$

where $\eta, \beta, \gamma, M, t_{xy}, t_z$ are real constants. More explicitly,

$$H = \sum_{\mathbf{k}} \eta[\sin k_x c^\dagger(\mathbf{k})\tau_x\sigma_z c(\mathbf{k}) - \sin k_y c^\dagger(\mathbf{k})\tau_y c(\mathbf{k})]$$

$$\begin{aligned}
& + \sum_{\mathbf{k}} (\beta + \gamma) \sin k_z (\cos k_y - \cos k_x) [c^\dagger(\mathbf{k}) \tau_x \sigma_x c(\mathbf{k})] \\
& + \sum_{\mathbf{k}} (-1) (\beta - \gamma) \sin k_z \sin k_x \sin k_y [c^\dagger(\mathbf{k}) \tau_x \sigma_y c(\mathbf{k})] \\
& + \sum_{\mathbf{k}} [M - t_{xy} (\cos k_x + \cos k_y) - t_z \cos k_z] [c^\dagger(\mathbf{k}) \tau_z c(\mathbf{k})], \tag{13}
\end{aligned}$$

where $c^\dagger = [c_{A,\uparrow}^\dagger, c_{B,\uparrow}^\dagger, c_{A,\downarrow}^\dagger, c_{B,\downarrow}^\dagger]$. In real space, the Hamiltonian becomes

$$\begin{aligned}
H & = \frac{\eta}{2} \sum_n [-i c_n^\dagger \tau_x \sigma_z c_{n+\hat{x}} + i c_n^\dagger \tau_y c_{n+\hat{y}} + h.c.] \\
& + \frac{(\beta + \gamma)}{4} \sum_n [-i c_n^\dagger \tau_x \sigma_x c_{n+\hat{y}+\hat{z}} - i c_n^\dagger \tau_x \sigma_x c_{n-\hat{y}+\hat{z}} + i c_n^\dagger \tau_x \sigma_x c_{n+\hat{x}+\hat{z}} + i c_n^\dagger \tau_x \sigma_x c_{n-\hat{x}+\hat{z}} + h.c.] \\
& + \frac{(\beta - \gamma)}{8} \sum_n [-i c_n^\dagger \tau_x \sigma_y c_{n+\hat{x}+\hat{y}+\hat{z}} - i c_n^\dagger \tau_x \sigma_y c_{n-\hat{x}-\hat{y}+\hat{z}} - i c_n^\dagger \tau_x \sigma_y c_{n+\hat{x}-\hat{y}-\hat{z}} - i c_n^\dagger \tau_x \sigma_y c_{n-\hat{x}-\hat{y}-\hat{z}} + h.c.] \\
& + M \sum_n c_n^\dagger \tau_z c_n - \frac{t_{xy}}{2} \sum_n [c_n^\dagger \tau_z c_{n+\hat{x}} + c_n^\dagger \tau_z c_{n+\hat{y}} + h.c.] - \frac{t_z}{2} \sum_n [c_n^\dagger \tau_z c_{n+\hat{z}} + h.c.], \tag{14}
\end{aligned}$$

where n indicates the lattice sites and $\hat{x}, \hat{y}, \hat{z}$ are the unit lattice vectors along x, y, z directions. η indicates the nearest neighbor hopping amplitudes in the xy plane, $(\beta + \gamma)$ denotes the next nearest neighbor hopping amplitudes in the yz and zx planes, and $(\beta - \gamma)$ indicates the hopping process along the body-diagonal direction of the cubic lattice. M indicates the on-site potential difference between the A and B orbitals, and t_{xy} (t_z) describes the hopping amplitude difference in different orbitals along the x, y directions (in the z direction).

Similarly, for the C_4 invariant system with $P = \pm\tau_0$, i.e., 7-th row of Table 1, we use

$$\begin{aligned}
f & = \eta \sin k_z (\sin k_x + i \sin k_y), \\
g & = [(\beta + \gamma) (\cos k_y - \cos k_x) + i (\beta - \gamma) \sin k_x \sin k_y], \\
a_5 & = M - t_{xy} (\cos k_x + \cos k_y) - t_z \cos k_z. \tag{15}
\end{aligned}$$

More explicitly,

$$\begin{aligned}
H & = \sum_{\mathbf{k}} \eta [\sin k_x \sin k_z c^\dagger(\mathbf{k}) \tau_x c(\mathbf{k}) - \sin k_y \sin k_z c^\dagger(\mathbf{k}) \tau_y \sigma_z c(\mathbf{k})] \\
& + \sum_{\mathbf{k}} (\beta + \gamma) (\cos k_y - \cos k_x) [c^\dagger(\mathbf{k}) \tau_y \sigma_x c(\mathbf{k})] \\
& + \sum_{\mathbf{k}} (-1) (\beta - \gamma) \sin k_x \sin k_y [c^\dagger(\mathbf{k}) \tau_y \sigma_y c(\mathbf{k})] \\
& + \sum_{\mathbf{k}} [M - t_{xy} (\cos k_x + \cos k_y) - t_z \cos k_z] [c^\dagger(\mathbf{k}) \tau_z c(\mathbf{k})], \tag{16}
\end{aligned}$$

In real space, the Hamiltonian becomes

$$\begin{aligned}
H = & -\frac{\eta}{4} \sum_n [c_n^\dagger \tau_x c_{n+\hat{x}+\hat{z}} - c_n^\dagger \tau_x c_{n-\hat{x}+\hat{z}} - c_n^\dagger \tau_y \sigma_z c_{n+\hat{y}+\hat{z}} + c_n^\dagger \tau_y \sigma_z c_{n-\hat{y}+\hat{z}} + h.c.] \\
& - \frac{(\beta + \gamma)}{2} \sum_n [c_n^\dagger \tau_y \sigma_x c_{n+\hat{x}} - c_n^\dagger \tau_y \sigma_x c_{n+\hat{y}} + h.c.] \\
& + \frac{(\beta - \gamma)}{4} \sum_n [c_n^\dagger \tau_y \sigma_y c_{n+\hat{x}+\hat{y}} - c_n^\dagger \tau_y \sigma_y c_{n+\hat{x}-\hat{y}} + h.c.] \\
& + M \sum_n c_n^\dagger \tau_z c_n - \frac{t_{xy}}{2} \sum_n [c_n^\dagger \tau_z c_{n+\hat{x}} + c_n^\dagger \tau_z c_{n+\hat{y}} + h.c.] - \frac{t_z}{2} \sum_n [c_n^\dagger \tau_z c_{n+\hat{z}} + h.c.], \quad (17)
\end{aligned}$$

where $(\beta + \gamma)$ indicates the nearest neighbor hopping amplitudes in the xy plane, $(\beta - \gamma)$ (η) denotes the next nearest neighbor hopping amplitudes in the xy (yz and zx) planes. M , t_{xy} , t_z have the same meaning as above. In both cases, we have chosen $\eta = 1$, $\beta = 2$, $\gamma = 1$, $t_z = 1$ while varying M and t_{xy} for the numerical computation.

-
- ¹ Hasan, M. Z., & Kane, C. L., Topological Insulators. *Rev. Mod. Phys.* **82**, 3045 (2010).
 - ² Qi, X. -L., & Zhang, S. -C., Topological Insulators and superconductors. *Rev. Mod. Phys.* **83**, 1057 (2011).
 - ³ Castro Neto, A. H., Guinea, F., Peres, N. M. R., Novoselov, K. S., & Geim, A. K., The electronic properties of graphene. *Rev. Mod. Phys.* **81**, 109 (2009).
 - ⁴ Murakami, S., Iso, S., Avishai, Y., Onoda, M., & Nagaosa, N., Tuning phase transition between quantum spin Hall and ordinary insulating phases. *Phys. Rev. B* **76**, 205304 (2007).
 - ⁵ Murakami, S., & Kuga, S. -i., Universal phase diagrams for the quantum spin Hall systems. *Phys. Rev. B* **78**, 165313 (2008).
 - ⁶ Murakami, S., Phase transition between the quantum spin Hall and insulator phases in 3D: emergence of a topological gapless phase. *New J. Phys.* **9**, 356 (2007).
 - ⁷ Xu, S. -Y., Xia, Y., Wray, L. A., Jia, S., Meier, F., Dil, J. H., Osterwalder, J., Slomski, B., Bansil, A., Lin, H., Cava, R. J., & Hasan, M. Z., Topological phase transition and texture inversion in a tunable topological insulator. *Science* **332**, 560-564 (2011).
 - ⁸ Sato, T., Segawa, K., Kosaka, K., Souma, S., Nakayama, K., Eto, K., Minami, T., Ando, Y., & Takahashi, T., Unexpected mass acquisition of Dirac fermions at the quantum phase transition of a topological insulator. *Nat. Phys.* **7**, 840 (2011).

- ⁹ Liu, Z. K., Zhou, B., Zhang, Y., Wang, Z. J., Weng, H. M., Prabhakaran, D., Mo, S. -K., Shen, Z. X., Fang, Z., Dai, X., Hussain, Z., & Chen, Y. L., Discovery of a Three-Dimensional Topological Dirac Semimetal, Na₃Bi. *Science* **343**, 864 (2014).
- ¹⁰ Xu, S. -Y., Liu, C., Kushwaha, S. K., Chang, T. -R., Krizan, J. W., Sankar, R., Polley, C. M., Adell, J., Balasubramanian, T., Miyamoto, K., Alidoust, N., Bian, G., Neupane, M., Belopolski, I., Jeng, H. -T., Huang, C. -Y., Tsai, W. -F., Lin, H., Chou, F. C., Okuda, T., Bansil, A., Cava, R. J., & Hasan, M. Z., Observation of a bulk 3D Dirac multiplet, Lifshitz transition, and nested spin states in Na₃Bi. *arXiv:1312.7624* (2014).
- ¹¹ Neupane, M., Xu, S. -Y., Sankar, R., Wan Alidoust, N., Bian, G., Liu, C., Belopolski, I., Chang, T. -R., Jeng, H. -T., Lin, H., Bansil, A., Chou, F., & Hasan, M. Z., Observation of a topological 3D Topological Dirac semimetal phase in high-mobility Cd₃As₂. *arXiv:1309.7892* (2014).
- ¹² Borisenko, S., Gibson, Q., Evtushinsky, D., Zabolotny, V., Buchner, B., & Cava, R. J., Experimental Realization of a Three-Dimensional Dirac Semimetal. *arXiv:1309.7978* (2014).
- ¹³ Jeon, S., Zhou, B. B., Gyenis, A., Feldman, B. E., Kimchi, I., Potter, A. C., Gibson, Q. D., Cava, R. J., Vishwanath, A., & Yazdani, A., Landau Quantization and Quasiparticle Interference in the Three-Dimensional Dirac Semimetals Cd₃As₂. *arXiv:1403.3446* (2014).
- ¹⁴ Young, S. M., Zaheer, S., Teo, J. C. Y., Kane, C. L., Mele, E. J., & Rappe, A. M., Dirac Semimetal in Three Dimensions. *Phys. Rev. Lett* **108**, 140405 (2012).
- ¹⁵ Steinberg, J. A., Young, S. M., Zaheer, S., Kane, C. L., Mele, E. J., & Rappe, A. M., Bulk Dirac Points in Distorted Spinels. *Phys. Rev. Lett* **112**, 036403 (2014).
- ¹⁶ Wang, Z., Sun, Y., Chen, X. Q., Franchini, C., Xu, G., Weng, H., Dai, X., & Fang, Z., Dirac semimetal and topological phase transitions in A₃Bi (A=Na, K, Rb). *Phys. Rev. B* **85**, 195320 (2012).
- ¹⁷ Wang, Z., Weng, H., Wu, Q., Dai, X., & Fang, Z., Three-dimensional Dirac semimetal and quantum transport in Cd₃As₂. *Phys. Rev. B* **88**, 125427 (2013).
- ¹⁸ Fang, C., Gilbert, M. J., Dai, X., & Bernevig, B. A., Multi-Weyl Topological Semimetals Stabilized by Point Group Symmetry. *Phys. Rev. Lett.* **108**, 266802 (2012).
- ¹⁹ Xu, G., Weng, H., Weng, Z., Dai, X., & Fang, Z., Chern Semimetal and the Quantized Anomalous Hall Effect in HgCr₂Se₄. *Phys. Rev. Lett* **107**, 186806 (2011).
- ²⁰ Fu, L., Kane, C. L., & Mele, E. J., Topological Insulators in Three Dimensions. *Phys. Rev. Lett.* **98**, 106803 (2007).

- ²¹ Moore, J. E., & Balents, L., Topological invariants of time-reversal-invariant band structures. *Phys. Rev. B* **75**, 121306(R) (2007).
- ²² Fu, L., & Kane, C. L., Topological insulators with inversion symmetry. *Phys. Rev. B* **76**, 045302 (2007).
- ²³ Teo, J. C. Y., Fu, L., & Kane, C. L., Surface states and topological invariants in three-dimensional topological insulators: Application to $\text{Bi}_{1-x}\text{Sb}_x$. *Phys. Rev. B* **78**, 045426 (2008).
- ²⁴ Hsieh, T. H., Lin, H., Liu, J., Duan, W., Bansil, A., & Fu, L., Topological crystalline insulators in the SnTe material class. *Nat. Comm.* **3**, 982 (2012).
- ²⁵ Wan, X., Turner, A. M., Vishwanath, A., & Savrasov, S. Y., Topological Semimetal and Fermi-Arc Surface States in the Electronic Structure of Pyrochlore Iridates. *Phys. Rev. B* **83**, 205101 (2011).
- ²⁶ Balents, L., Viewpoint: Weyl electrons kiss. *Physics* **4**, 36 (2011).
- ²⁷ Witczak-Krempa, W., Chen, G., Kim, Y. B., Balents, L., Correlated Quantum Phenomena in the Strong Spin-Orbit Regime. *Annu. Rev. Condens. Matter Phys.* **5**, 57-82 (2014).
- ²⁸ Goswami, P., & Chakravarty, S., Quantum Criticality between Topological and Band Insulators in 3+1 Dimensions. *Phys. Rev. Lett* **107**, 196803 (2011).
- ²⁹ Isobe, H., & Nagaosa, N., Theory of a quantum critical phenomenon in a topological insulator: (3+1)-dimensional quantum electrodynamics in solids. *Phys. Rev. B* **86**, 165127 (2012).
- ³⁰ Isobe, H., & Nagaosa, N., Renormalization group study of electromagnetic interaction in multi-Dirac-node systems. *Phys. Rev. B* **87**, 205138 (2013).
- ³¹ Hosur, P., Parameswaran, S. A., & Vishwanath, A., Charge Transport in Weyl Semimetals. *Phys. Rev. Lett* **108**, 046602 (2012).
- ³² González, F. J., Guinea, F., & Vozmediano, M. A. H., Non-Fermi liquid behavior of electrons in the half-filled honeycomb lattice (A renormalization group approach). *Nucl. Phys. B* **424**, 595 (1994).
- ³³ Kotov, V. N., Uchoa, B., Pereira, V. M., Guinea, F., & Castro Neto, A. H., Electron-Electron Interactions in Graphene: Current Status and Perspectives. *Rev. Mod. Phys.* **84**, 1067 (2012).
- ³⁴ Son, D. T., Quantum critical point in graphene approached in the limit of infinitely strong Coulomb interaction. *Phys. Rev. B* **75**, 235423 (2007).
- ³⁵ Moon, E. -G., Xu, C., Kim, Y. B., & Balents, L., Non-Fermi-Liquid and Topological States with Strong Spin-Orbit Coupling. *Phys. Rev. Lett.* **111**, 206401 (2013).

- ³⁶ Yang, B. -J., Bahramy, M. S., Arita, R. , Isobe, H. , Moon, E. -G., & Nagaosa, N., Theory of Topological Quantum Phase Transitions in 3D Noncentrosymmetric Systems. *Phys. Rev. Lett.* **110**, 086402 (2013).
- ³⁷ Yang, B. -J., Moon, E. -G., Isobe, H. , & Nagaosa, N., Quantum Criticality of Topological Phase Transitions in 3D Interacting Electronic Systems. *Unpublished*(2014).

Acknowledgements

We greatly appreciate the stimulating discussion with Xi Dai. We are grateful for support from the Japan Society for the Promotion of Science (JSPS) through the ‘Funding Program for World-Leading Innovative R&D on Science and Technology (FIRST Program)

C_n	$ P $	$(u_{A,\uparrow}, u_{B,\uparrow})$	$f(k_{\pm}, k_z)$	$g(k_{\pm}, k_z)$	2D topological invariant	$H_{\text{Dirac}}(\mathbf{q})$	Materials
C_2	τ_z	—	—	—	—	Not allowed	
C_2	τ_0	—	—	—	—	Not allowed	
C_3	τ_z	$(e^{i\pi}, e^{i\frac{\pi}{3}})$	βk_+	γk_-	$\nu_{2D} = 1$	Linear Dirac	$\text{Na}_3\text{Bi}^{16}$
C_3	τ_0	$(e^{i\pi}, e^{i\frac{\pi}{3}})$	$\beta k_z k_+ + \gamma k_-^2$	$\eta k_z k_- + \xi k_+^2$	$\nu_{2D} = 0$	Linear Dirac	
C_4	τ_z	$(e^{i\frac{3\pi}{4}}, e^{i\frac{\pi}{4}})$	ηk_+	$\beta k_z k_+^2 + \gamma k_z k_-^2$	$n_M = \pm 1$	Linear Dirac	$\text{Cd}_3\text{As}_2^{17}$
C_4	τ_0	$(e^{i\frac{3\pi}{4}}, e^{i\frac{\pi}{4}})$	$\eta k_z k_+$	$\beta k_+^2 + \gamma k_-^2$	$n_M = 2\text{sgn}(\beta - \gamma)$	Linear Dirac	
C_6	τ_z	$(e^{i\frac{\pi}{2}}, e^{i\frac{\pi}{6}})$	βk_+	$\gamma k_z k_+^2$	$n_M = \pm 1$	Linear Dirac	
C_6	τ_0	$(e^{i\frac{\pi}{2}}, e^{i\frac{\pi}{6}})$	$\beta k_z k_+$	γk_+^2	$n_M = \pm 2$	Linear Dirac	
C_6	τ_z	$(e^{i\frac{5\pi}{6}}, e^{i\frac{\pi}{2}})$	βk_+	$\gamma k_z k_-^2$	$n_M = \pm 1$	Linear Dirac	
C_6	τ_0	$(e^{i\frac{5\pi}{6}}, e^{i\frac{\pi}{2}})$	$\beta k_z k_+$	γk_-^2	$n_M = \pm 2$	Linear Dirac	
C_6	τ_z	$(e^{i\frac{5\pi}{6}}, e^{i\frac{\pi}{6}})$	$\eta k_z k_+^2$	$\beta k_+^3 + \gamma k_-^3$	$n_M = 3\text{sgn}(\beta - \gamma)$	Quadratic Dirac	
C_6	τ_0	$(e^{i\frac{5\pi}{6}}, e^{i\frac{\pi}{6}})$	ηk_+^2	$\beta k_z k_+^3 + \gamma k_z k_-^3$	$n_M = \pm 2$	Quadratic Dirac	

Classification table for 3D topological Dirac semimetals. Classification table for 3D topological Dirac semimetals obtained by an accidental band crossing in systems having C_n rotational symmetry with respect to the z axis. Here $C_n = \text{diag}[u_{A,\uparrow}, u_{B,\uparrow}, u_{A,\downarrow} = u_{A,\uparrow}^*, u_{B,\downarrow} = u_{B,\uparrow}^*]$ and β, γ, η, ξ are complex numbers. For compact presentation, $u_{A,\uparrow}$ and $u_{B,\uparrow}$ are arranged in a way that $0 < \arg(u_{B,\uparrow}) < \arg(u_{A,\uparrow}) \leq \pi$. ν_{2D} (n_M) indicates the 2D Z_2 invariant (mirror Chern number) defined on the $k_z = 0$ plane. ($n_M = \nu_{2D} \bmod 2$.) The 2×2 Hamiltonian $h_{\uparrow\uparrow}(\mathbf{k}) = f(\mathbf{k})\tau_+ + f^*(\mathbf{k})\tau_- + a_5(\mathbf{k})\tau_z$. In the case of $h_{\uparrow\downarrow}(\mathbf{k})$, $h_{\uparrow\downarrow}(\mathbf{k}) = g(\mathbf{k})\tau_x$ when $P = \pm\tau_z$ while $h_{\uparrow\downarrow}(\mathbf{k}) = g(\mathbf{k})\tau_y$ when $P = \pm\tau_0$. The leading order terms of $f(\mathbf{k})$ and $g(\mathbf{k})$ are shown in the table. $H_{\text{Dirac}}(\mathbf{q})$ describes the effective Hamiltonian near the bulk Dirac point, which is either $H_{\text{Dirac}}(\mathbf{q}) = v_x q_x \Gamma_1 + v_y q_y \Gamma_2 + v_z q_z \Gamma_3$ (Linear Dirac) or $H_{\text{Dirac}}(\mathbf{q}) = v_x (q_x^2 - q_y^2) \Gamma_1 + 2v_y q_x q_y \Gamma_2 + v_z q_z \Gamma_3$ (Quadratic Dirac) where $\Gamma_{1,2,3}$ are mutually anticommuting 4×4 Gamma matrices and $v_{x,y,z}$ are real constants. Here the momentum \mathbf{q} is measured with respect to the bulk Dirac point.

C_n	$ P $	$u_{A,\uparrow}$	$f(k_{\pm}, k_z)$	$g_z(k_{\pm}, k_z)$	$H_{\text{Dirac}}(\mathbf{q})$	Material
C_2	τ_x	$e^{i\frac{\pi}{2}}$	$k_z F_1^{(1)}(k_{x,y}) - iF_2^{(1)}(k_{x,y})$	$\alpha k_x + \beta k_y$	Linear Dirac	Distorted Spinels ¹⁵
C_3	τ_x	—	—	—	Not allowed	
C_4	τ_x	$e^{\pm i\frac{\pi}{4}}$	$F_1^{(2)}(k_{x,y}) - ik_z F_2^{(2)}(k_{x,y})$	αk_{\pm}	Linear Dirac	BiO ₂ ¹⁴
C_6	τ_x	$e^{\pm i\frac{\pi}{6}}$	$k_z F_1^{(3)}(k_{x,y}) + iF_2^{(3)}(k_{x,y})$	αk_{\pm}	Linear Dirac	
C_6	τ_x	$e^{i\frac{3\pi}{6}}$	$k_z F_1^{(3)}(k_{x,y}) + iF_2^{(3)}(k_{x,y})$	$F_3^{(3)}(k_{x,y}) + iF_4^{(3)}(k_{x,y})$	Cubic Dirac	

Classification table for 3D Dirac SMs with a Dirac point at a TRIM on the rotation axis. Classification table for 3D topological Dirac semimetals in systems having C_n rotational symmetry with respect to the z axis when $P = \pm\tau_x$. In this Dirac SM phase, the location of the 3D Dirac point is fixed either at the center or the edge of the rotation axis, i.e., at a TRIM on the rotation axis. Here $C_n = \text{diag}[u_{A,\uparrow}, u_{B,\uparrow}, u_{A,\downarrow}, u_{B,\downarrow}] = \text{diag}[u_{A,\uparrow}, -u_{A,\uparrow}, u_{A,\uparrow}^*, -u_{A,\uparrow}^*]$ and α, β are complex numbers. For compact presentation, $\arg(u_{A,\uparrow})$ is fixed to be $-\frac{\pi}{2} \leq \arg(u_{A,\uparrow}) \leq \frac{\pi}{2}$. But the same result holds even if $\arg(u_{A,\uparrow})$ is shifted by π . The real functions $F^{(1,2,3)}$ are given by $F_{i=1,2}^{(1)} = c_i^{(1)}k_x + d_i^{(1)}k_y$, $F_{i=1,2}^{(2)} = c_i^{(2)}(k_x^2 + k_y^2) + d_i^{(2)}k_x k_y$, $F_{i=1,2,3,4}^{(3)} = c_i^{(3)}(k_+^3 + k_-^3) + id_i^{(3)}(k_+^3 - k_-^3)$ where $c_i^{(1,2,3)}$ and $d_i^{(1,2,3)}$ are real constants. The 2×2 Hamiltonian $h_{\uparrow\uparrow}(\mathbf{k}) = f(\mathbf{k})\tau_+ + f^*(\mathbf{k})\tau_- + a_1(\mathbf{k})\tau_z$ where $a_1(\mathbf{k}) = vk_z$ with a real constant v , and $h_{\uparrow\downarrow}(\mathbf{k}) = g_z(\mathbf{k})\tau_z$. The leading order terms of $f(\mathbf{k})$ and $g_z(\mathbf{k})$ are shown in the table. $H_{\text{Dirac}}(\mathbf{q})$ describes the effective Hamiltonian near the bulk Dirac point, which is either $H_{\text{Dirac}}(\mathbf{q}) = v_x q_x \Gamma_1 + v_y q_y \Gamma_2 + v_z q_z \Gamma_3$ (Linear Dirac) or $H_{\text{Dirac}}(\mathbf{q}) = v_x (q_+^3 + q_-^3) \Gamma_1 + iv_y (q_+^3 - q_-^3) \Gamma_2 + v_z q_z \Gamma_3$ (Cubic Dirac) where the momentum \mathbf{q} is measured with respect to the bulk Dirac point with $q_{\pm} = q_x \pm iq_y$. Here $\Gamma_{1,2,3}$ are mutually anticommuting 4×4 Gamma matrices and $v_{x,y,z}$ are real constants.

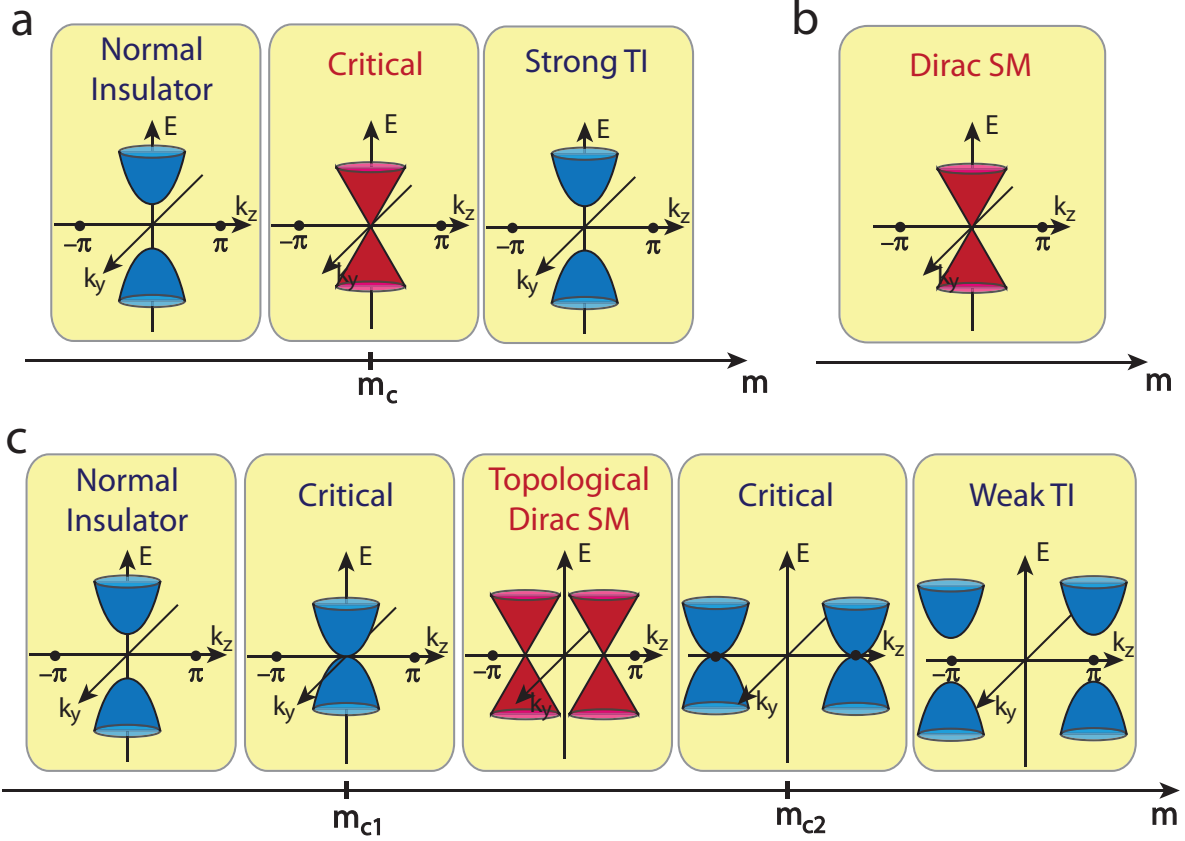


FIG. 1: **Creation of a topological Dirac semimetal (SM) via accidental gap closings.** (a) The phase transition induced by an ABC when a single control parameter m is varied in systems with the TRS and IS but lacking the rotation symmetry. The 3D Dirac fermion appears only at the critical point $m = m_c$ and the ABC mediates the transition between a normal insulator and a strong topological insulator (TI). When an additional uniaxial rotational symmetry is included, two different phase diagrams can be obtained as shown in (b) and (c). Here we choose the k_z axis as the axis for the n -fold rotation. (b) The Dirac SM persists irrespective of m . The Dirac point locates at a TRIM on the rotation axis. The Dirac SM in Table 2 corresponds to this case. (c) A stable topological Dirac SM phase appears when $m_{c1} < m < m_{c2}$, which mediates the transition between a normal insulator and a weak TI. Here a pair of bulk Dirac points, each of which has four-fold degeneracy at the gapless point, exist along the rotation axis and approach the Brillouin zone (BZ) boundary as m increases. The Dirac SM in Table 1 corresponds to this case. At the quantum critical points ($m = m_{c1}$ or $m = m_{c2}$), the energy dispersion along the k_z direction is quadratic while the dispersion along the k_x and k_y directions is linear (linear Dirac SM) or quadratic (quadratic Dirac SM) or cubic (cubic Dirac SM).

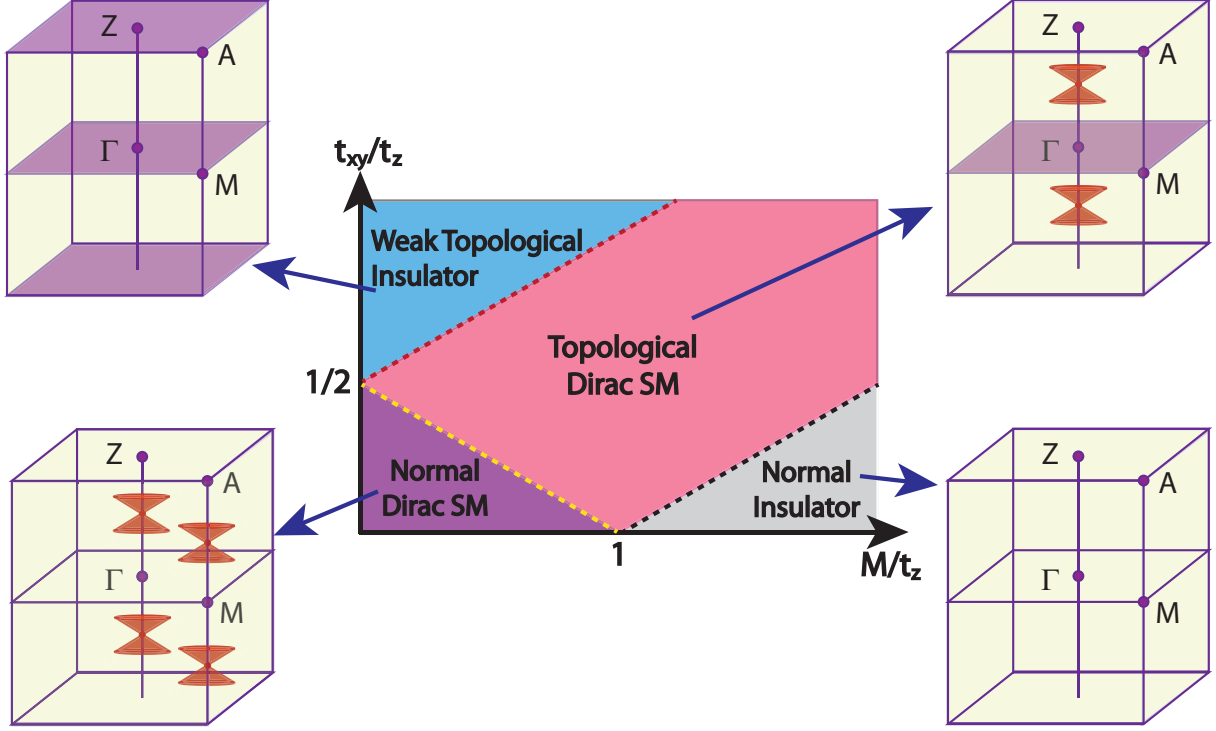


FIG. 2: **Generic phase diagram of the system with the time-reversal, inversion, and rotation symmetries.** The phase diagram is obtained by numerically solving the lattice Hamiltonians in Equations (14) and (17), both of which lead to the same phase diagram. Here M indicates the on-site energy difference between two orbitals and t_{xy} (t_z) describes the hopping amplitude along the direction perpendicular (parallel) to the rotation axis. For each phase, the location of the 3D bulk Dirac point in the first BZ, if it is present, is indicated by the red symbol having the shape of a Dirac cone. When the two dimensional (2D) plane with $k_z = 0$ or $k_z = \pi$ possesses a nontrivial 2D topological invariant, such as Z_2 invariant (ν_{2D}) or the mirror Chern number (n_M), the corresponding plane is colored in purple. If any of these 2D planes carries a nonzero 2D topological invariant, the surface of the material, which is parallel to the axis of the rotation, supports 2D surface Dirac cones. A gap-closing happens at the Γ (Z) point on the black (red) dotted line while a gap-closing occurs at the M point on the yellow dotted line.

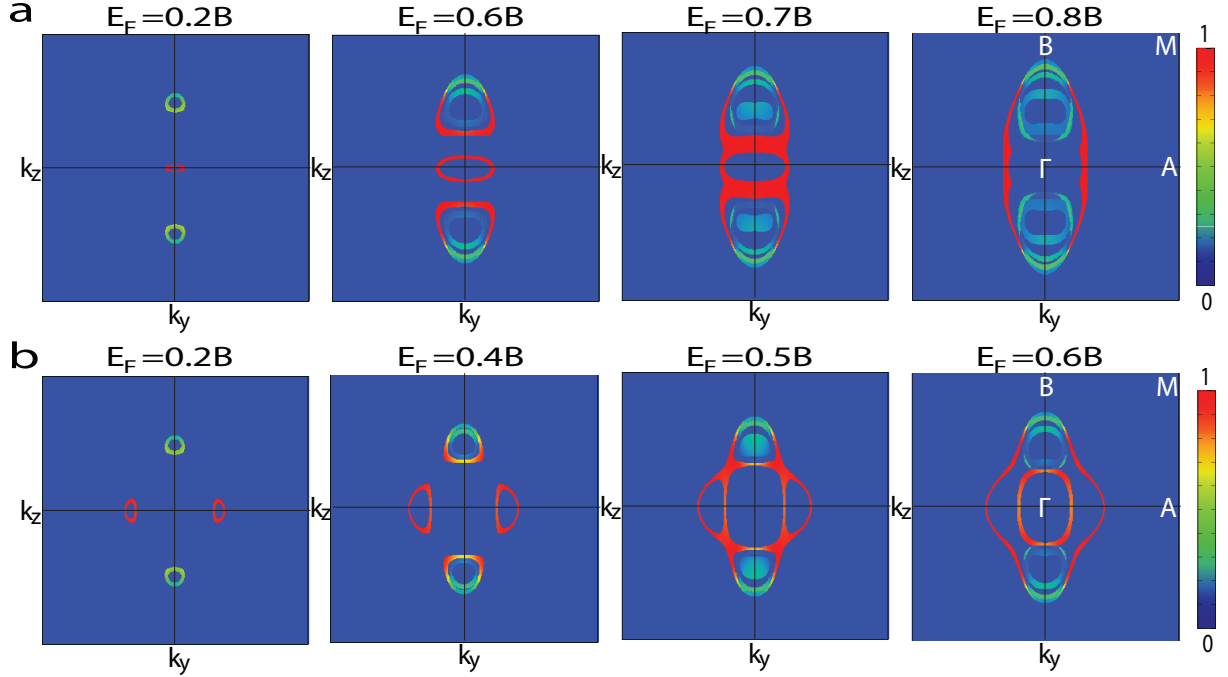


FIG. 3: Evolution of the Fermi surface of a film whose surface normal direction is parallel to $[100]$ direction as a function of the Fermi energy. The wave function amplitudes confined within the first five layers from the top surface are plotted for the states touching the Fermi level (E_F). To obtain the Fermi surface we have solved numerically the lattice Hamiltonian in Equations (14) and (17). (a) For a topological Dirac semimetal with C_4 symmetry, which has $\nu_{2D} = 1$ on the $k_z = 0$ plane. The closed loop at the center of the surface BZ is from a 2D surface Dirac point at the Γ point. Two 3D bulk Dirac cones also produce finite intensity symmetrically on the k_z axis. As E_F increases, the closed loop due to the 2D Dirac point deforms to a pair of Fermi arcs connected to the bulk states. (b) For a topological Dirac semimetal with C_4 symmetry, which has $n_m = 2$ on the $k_z = 0$ plane. The two closed loops on the k_y axis are due to two 2D Dirac points localized on the surface. As E_F increases, the closed loops due to 2D Dirac cones turn into four Fermi arcs. In both (a) and (b), the 3D bulk Dirac fermions show the linear dispersion in the momentum space. Hence, the number of surface Fermi arcs is solely determined by the 2D topological invariant on the $k_z = 0$ plane independent of the dispersion of the bulk Dirac fermions.